
DATA-DRIVEN GENERATION OF PLAUSIBLE TISSUE GEOMETRIES FOR REALISTIC PHOTOACOUSTIC IMAGE SYNTHESIS

Melanie Schellenberg *

Computer Assisted Medical Interventions (CAMI)
Heidelberg, Germany
melanie.schellenberg@dkfz.de

Janek Gröhl * [†]

Computer Assisted Medical Interventions (CAMI)
Heidelberg, Germany

Kris Dreher *

Computer Assisted Medical Interventions (CAMI)
Heidelberg, Germany

Niklas Holzwarth *

Computer Assisted Medical Interventions (CAMI)
Heidelberg, Germany

Minu D. Tizabi *

Computer Assisted Medical Interventions (CAMI)
Heidelberg, Germany

Alexander Seitel *

Computer Assisted Medical Interventions (CAMI)
Heidelberg, Germany

Lena Maier-Hein *^{‡§}

Computer Assisted Medical Interventions (CAMI)
Heidelberg, Germany
l.maier-hein@dkfz-heidelberg.de

March 1, 2025

ABSTRACT

Photoacoustic tomography (PAT) has the potential to recover morphological and functional tissue properties such as blood oxygenation with high spatial resolution and in an interventional setting. However, decades of research invested in solving the inverse problem of recovering clinically relevant tissue properties from spectral measurements have failed to produce solutions that can quantify tissue parameters robustly in a clinical setting. Previous attempts to address the limitations of model-based approaches with machine learning were hampered by the absence of labeled reference data needed for supervised algorithm training. While this bottleneck has been tackled by simulating training data, the domain gap between real and simulated images remains a huge unsolved challenge. As a first step to address this bottleneck, we propose a novel approach to PAT data simulation, which we refer to as "learning to simulate". Our approach involves subdividing the challenge of generating plausible simulations into two disjoint problems: (1) Probabilistic generation of realistic tissue morphology, represented by *semantic segmentation maps* and (2) pixel-wise assignment of corresponding optical and acoustic properties. In the present work, we focus on the first challenge. Specifically, we leverage the concept of Generative Adversarial Networks (GANs) trained on semantically annotated medical imaging data to generate plausible tissue geometries. According to an initial *in silico* feasibility study our approach is well-suited for contributing to realistic PAT image synthesis and could thus become a fundamental step for deep learning-based quantitative PAT.

Keywords Photoacoustic imaging, Photoacoustic tomography, Optoacoustic tomography, Optoacoustic imaging, Deep learning, Synthetic data, Generative adversarial networks

* German Cancer Research Center (DKFZ)

[†] now at Cancer Research UK, Cambridge Institute, Cambridge, U.K.

[‡] Medical Faculty, Heidelberg University, Heidelberg, Germany

[§] Faculty of Mathematics and Computer Science, Heidelberg University, Heidelberg, Germany

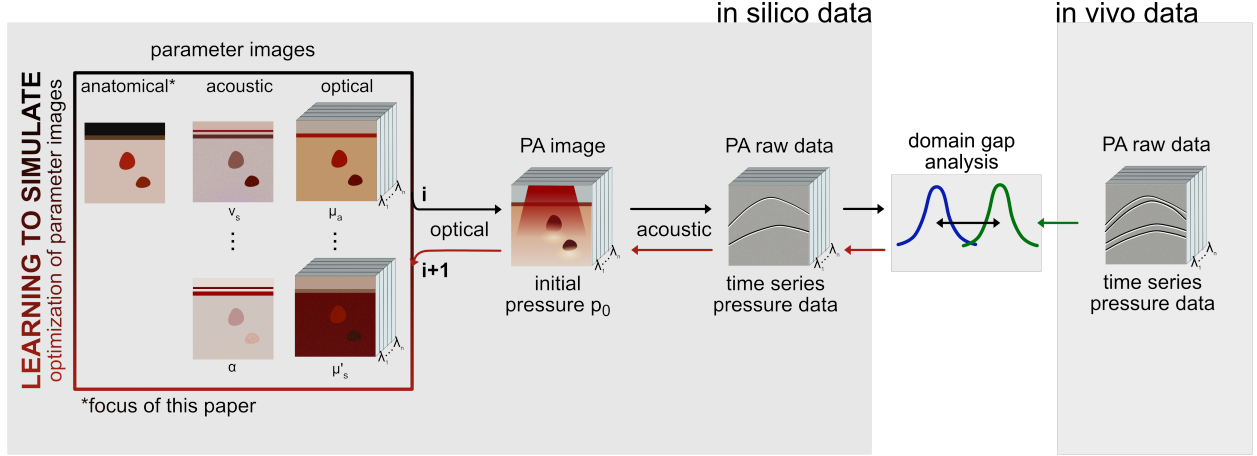


Figure 1: Our data-driven approach to quantitative photoacoustic tomography (NS-qPAT): We consider image formation (black arrows) and image decoding (red arrows) in one joint framework. The core of our concept is the explicit disentanglement of the different factors that contribute to image formation. These include anatomical, acoustic, and optical tissue parameters, all of which are represented by *parameter images*. The optical inverse problem is phrased as the recovery of these parameter images from the initial pressure images. The acoustic inverse problem relates to the reconstruction of the initial pressure images from the recorded raw time series pressure data. Our concept involves a machine learning-driven approach for the generation of the parameter images (shown in Fig. 2 for the anatomical parameter images), to close the domain gap between simulated and real measurements.

1 Introduction

Multispectral photoacoustic tomography (PAT) is an emerging medical imaging modality that provides morphological and functional tissue information with high contrast and spatial resolution in tissue depths up to several centimeters [1, 2]. Despite recent successes, numerous PAT applications [3] are not yet feasible in clinical settings. One of the primary obstacles related to clinical translation of PAT in these scenarios is that the absolute concentration of different absorbers, referred to as chromophores, cannot be quantified reliably. Even though the initial pressure distribution reconstructed from measured PAT raw data is proportional to the optical absorption coefficient of chromophores, it is also proportional to the light fluence which, in turn, is highly dependent on the distribution of chromophores and scatterers within the tissue. Consequently, quantification of chromophore concentrations from the underlying initial pressure distribution is an ill-posed inverse problem (*optical inverse problem*). Current model-based quantification approaches do not yield accurate results in clinical settings, mainly due to assumptions that do not hold in the clinical context [4, 5]. Machine learning-based solutions have recently been proposed as an alternative approach to model-based quantitative PAT (qPAT) [6, 7, 8]. Here, the absence of a reliable reference method for generating annotated training data was addressed by simulating training data with ground truth-underlying tissue properties. While these works obtained very encouraging results *in silico*, the data-driven approaches to qPAT tend to fail in realistic scenarios, probably due to the domain gap between real and simulated data [7, 9].

We address this challenge with a novel approach, named after the corresponding European Research Council (ERC) grant “NEURAL SPICING” (short: NS). NS-qPAT systematically combines established knowledge from biomedicine and physics with modern machine learning concepts to enable qPAT. The concept is based on two core components: A physics-based simulation framework for virtual spectral imaging and a neural network-based decoding framework that leverages both simulated data and real data to learn the recovery of relevant tissue properties from measurement data. Here, image synthesis and decoding are considered in one joint framework that explicitly disentangles all the different optical, acoustic, and geometric tissue properties that contribute to image formation (see Fig. 1).

In this broader research context, the contribution of this paper focuses on the realistic simulation of PAT data. Concretely, we present a simulation concept that leverages real medical imaging data to optimize the realism of tissue geometries that serve as a basis for PAT image synthesis (*anatomical* parameter images in Fig. 1). The following sections present our approach to synthetically generate tissue geometries as well as our initial feasibility study to validate this approach.

2 Material and methods

The ensuing sections present the proposed framework for "learning to simulate" (cf. Sect. 2.1), the specific approach to data-driven learning of plausible tissue geometries (cf. Sect. 2.2), as well as the initial feasibility study conducted to validate the latter (cf. Sect. 2.3).

2.1 "Learning to simulate" framework

In our approach, the problem of qPAT is formulated as a decoding task in which neural networks are applied to convert measurements pixel-wise (in 3D also referred to as voxel-wise) to underlying parameter images. In this context, image synthesis and decomposition are considered together as one joint problem. While previous approaches to deep learning-based qPAT have focused on solving the quantification problem directly, our approach relies on the explicit disentanglement and an analysis of the direct dependencies of all of the parameters that are relevant for the image formation (cf. Fig. 1). These parameters are represented by *parameter images* and comprise three classes: anatomical, optical, and acoustic parameters. The anatomical parameters describe the anatomy of different tissue types and therefore the spatially-resolved concentration of chromophores. Optical parameters, such as the absorption (μ_a) and scattering (μ_s) coefficients and acoustic parameters, such as the speed of sound (v_s), specify the molecular information relevant for the optical and acoustic image formation process, respectively.

A core component of NS-qPAT is the simulation framework. While previous simulation approaches have been purely model-based [10], a key feature of our concept is the fact that we leverage real data to learn parameter images in a data-driven manner. In this work, we concentrate on the realism of tissue geometries, hence the *anatomical parameter images*.

2.2 Learning tissue geometries

Recent success stories in the field of machine learning [11, 12, 13] have shown the high potential of GANs [14] in synthesizing realistic content. In the present work, we leverage GANs for synthetic PAT image generation in the following 5-step process (cf. Fig. 2).

- (a) **Image acquisition:** Acquisition/Gathering of tomographic 2D or 3D images of the target anatomy with any modality, such as computed tomography (CT), magnetic resonance imaging (MRI), ultrasound (US), and PAT.
- (b) **Image annotation:** Generation of semantic segmentations reflecting the format of the desired anatomical parameter images (see Fig. 2 for an example). Specifically, the input images are classified pixel-wise in a way that different classes present structures with systematically different acoustic and/or optical properties. In the case of forearm images, for example, the tissue classes veins, arteries, skin, and background tissue are labeled.
- (c) **Training of Generative Adversarial Network (GAN):** A GAN is trained to generate anatomical parameter images, resembling those in the training data set. Generally, a GAN consists of two networks, a generator and a discriminator network [14]. The generator network enables the generation of fake data. In particular, it learns to map a low-dimensional latent space, such as Gaussian distributed random noise, to a high-dimensional output, such as high-resolution synthetic images, with a data distribution identical to the real training data distribution. In contrast, the discriminator network is a classifier that learns to distinguish the real data from fake data. As the networks are competitors that continuously trigger mutual improvement, the optimization of both networks leads to generated realistic synthetic data. In our current framework, we apply the deep convolutional GAN [15] as it is a particularly preferred architecture for image synthesis [16].
- (d) **Image generation and post-processing:** The trained GAN is used to generate plausible anatomical parameter images (semantic segmentation maps). A plausibility check can be performed to remove generated images with anatomically implausible properties.
- (e) **Generation of optical and acoustic parameter images:** Based on the geometrical information, the remaining (optical and acoustic) parameter images are generated (typically also in a probabilistic manner).

The proposed workflow allows leveraging geometric information accessible from other modalities and directly addresses the fact that tissue geometries are relatively easy to label, while there is no reliable reference method for assigning acoustic/optical properties. The following section presents the first feasibility study we conducted to investigate the potential of the approach for deep learning-based solving of the optical inverse problem. Implementation details of our first prototype can be found in section 2.3.3.

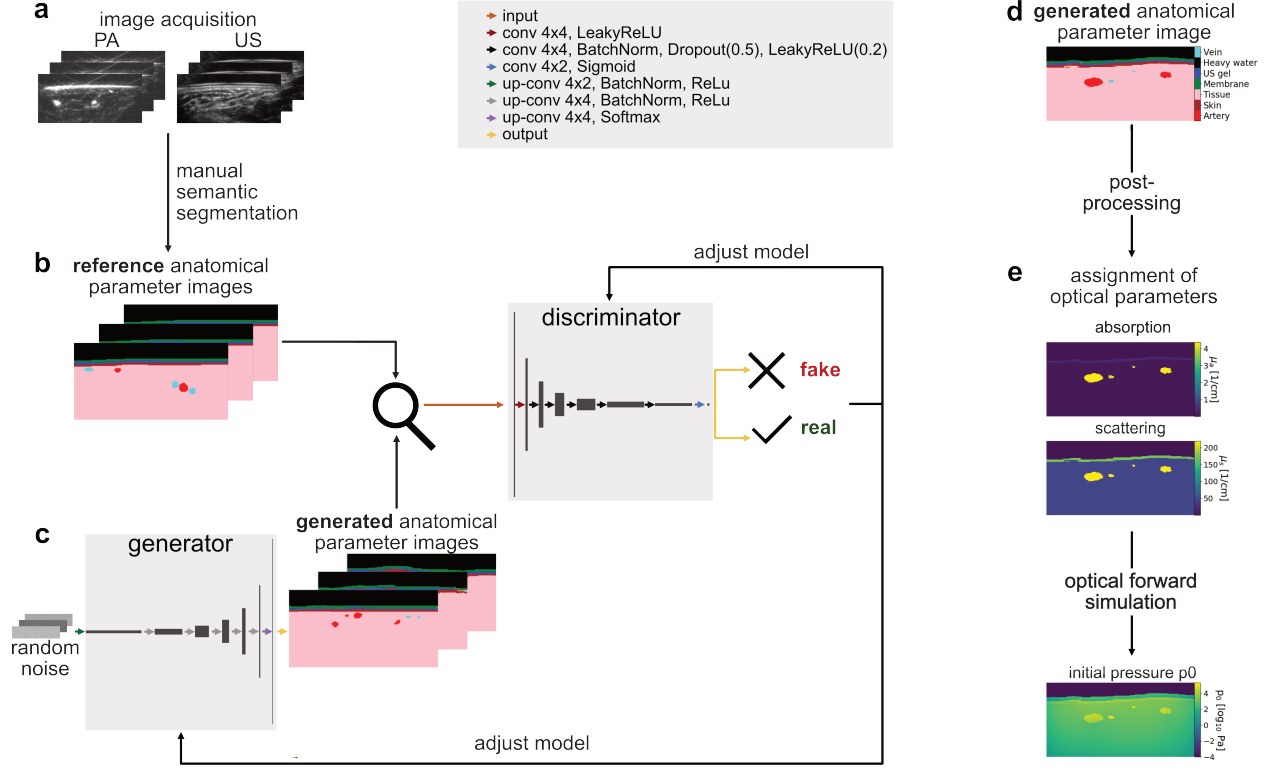


Figure 2: Concept for data-driven generation of synthetic photoacoustic tomography (PAT) training data. (*Left*) (a) Medical images related to the tissue geometry (here PAT co-registered to ultrasound (US) data) are (b) semantically segmented. These reference *anatomical parameter images* are used to train a (c) Generative Adversarial Network (GAN) for the generation of anatomical parameter images. While the generator network learns to generate realistic parameter images representing tissue geometry, the discriminator network learns to distinguish real from fake ones. The optimization of the competing networks leads to generated realistic segmentation masks with a data distribution identical to the data distribution of real segmentation masks. (*Right*) GAN-based simulation of PAT data. The simulation of a new training image comprises the generation of (d) an anatomical parameter image as well as (e) corresponding optical (and depending on the application also acoustic) parameter images leveraging the anatomical knowledge.

2.3 Experiments

The purpose of the experiments was to assess the benefit of our data-driven approach to the generation of tissue geometries. We compared our method (*GAN-based*) to both an approach leveraging literature knowledge for model-based generation of tissue geometries (*literature-based*) and an approach directly utilizing annotated semantic segmentation masks of real PAT measurements (*annotation-based*). The following sections present the corresponding data sets - namely the baseline data set (cf. Sect. 2.3.1), the reference annotation data set (cf. Sect. 2.3.2), the GAN-based data set generated with our approach (cf. Sect. 2.3.3) - as well as our strategy for comparative validation (cf. Sect. 2.3.4).

2.3.1 Literature-based generation of tissue geometries

The literature-based tissue geometries were generated using literature values of anatomical tissue parameters of different tissue classes of a human forearm including epidermis, dermis, muscle background, arteries, and veins. Aiming to achieve a realistic distribution of vessels, we investigated the real PAT measurements (cf. Sect. 2.3.2). The probabilities of the amount of arteries and veins in the data set were analysed (cf. Table 1) and a Poisson distribution was fitted to each distribution, respectively. The amount of vessels of one forearm model was determined by sampling from the two distributions. The underlying geometrical values, such as the size and location of a vessel, are based on an internally developed forearm tissue model in previous work [10, 17]. Using the Monte Carlo model implementation "Monte Carlo eXtreme" [18] included in the SIMPA toolkit multispectral absorption coefficient and initial pressure distributions (256 x 128 pixels, resolution $\Delta x = \Delta y = 0.16$ mm) were simulated in 16 wavelengths ranging from 700 - 850 nm in steps of

10 nm with optical tissue parameters that were chosen according to literature values of a human forearm [19]. Figure 3 (*literature* column, b-d) shows a randomly chosen semantic segmentation mask of the literature-based data set.

| # vessels | P(arteries) | P(veins) |
|-----------|-------------|----------|
| 0 | - | 10/60 |
| 1 | 7/60 | 16/60 |
| 2 | 19/60 | 13/60 |
| 3 | 16/60 | 15/60 |
| 4 | 11/60 | 2/60 |
| 5 | 4/60 | 2/60 |
| 6 | 2/60 | 1/60 |
| 7 | - | 1/60 |
| 8 | 1/60 | - |

Table 1: Probabilities (P) of the amount (#) of arteries and veins in the measured PAT data set (cf. Sect. 2.3.2) consisting of 60 images.

2.3.2 Annotation-based generation of tissue geometries

As a reference to realistic PAT segmentation masks, we used semantic segmentation masks of 60 pairs of US and PAT forearm images of ten healthy human volunteers. These image pairs were acquired using the Multispectral optoacoustic tomography (MSOT) Acuity Echo device (iThera Medical, Munich, Germany) with the consent of all volunteers and in compliance with relevant regulations. Static freehand scans of roughly 30 seconds at three positions at the right and left forearm of every volunteer were acquired following an acquisition protocol [20]. While the US images were reconstructed using a backprojection algorithm by the MSOT device itself, the PAT images were reconstructed using a Delay-And-Sum (DAS) algorithm within the Medical imaging interaction toolkit (MITK) [21]. The different reconstructions of PAT images enabled post-processing in three steps. First, the multispectral PAT images were corrected for laser pulse energy variations of the MSOT device. Each PAT image was divided by the respective laser pulse energy. Secondly, to account for the different fields of view of PAT and US resulting from the different reconstruction algorithms used, the PAT images were cropped, such that a co-registration with the US images was enabled. Thirdly, the image pairs were divided into four sub-scans of approximately eight seconds each. Every sub-scan was averaged pixel-wise and the resulting image pair with the sharpest edges in the US image according to the averaged calculated image gradient was selected. Following a detailed annotation protocol [20], these selected image pairs were semantically segmented by domain experts into the following classes: artery, vein, skin, muscle background tissue, US gel, transducer membrane, and transducer head. Based on these reference semantic segmentation masks, which are intended to include realistic anatomical parameters, the absorption coefficient, and initial pressure distributions were simulated with the SIMPA toolkit using the same simulation properties as described in section 2.3.1. Figure 3 (*annotation* column, b-d) shows a randomly chosen example of the annotation-based data set.

2.3.3 GAN-based generation of tissue geometries

While the annotation-based approach potentially yields the most accurate tissue geometries, it does not scale well due to the need for manual annotations. To compensate for the data sparsity, we propose a GAN-based approach that generates further plausible geometries by leveraging the existing ones. Based on the presented annotation-based data set (cf. Sect. 2.3.2), the proposed concept for data-driven tissue generation was implemented as follows: A deep convolutional GAN architecture shown in Figure 2 was trained on 48 of the reference annotations (not included in any test data). The hyperparameters (cf. Tab. 2) were determined by applying a grid search on the training data. With this generative model trained, 2428 diverse anatomical parameter images were generated. In a manual post-processing step, images that did not look anatomically plausible according to domain experts (e.g., featuring a non-continuous skin layer) were excluded, which yielded 490 GAN-based anatomical parameter images in total. The optical properties were assigned based on the generated segmentation masks and the initial pressure distribution was simulated with the SIMPA toolkit using the same simulation properties as described in section 2.3.1. Figure 3 (*GAN* column, b-d) shows a randomly chosen example of this GAN-based data set.

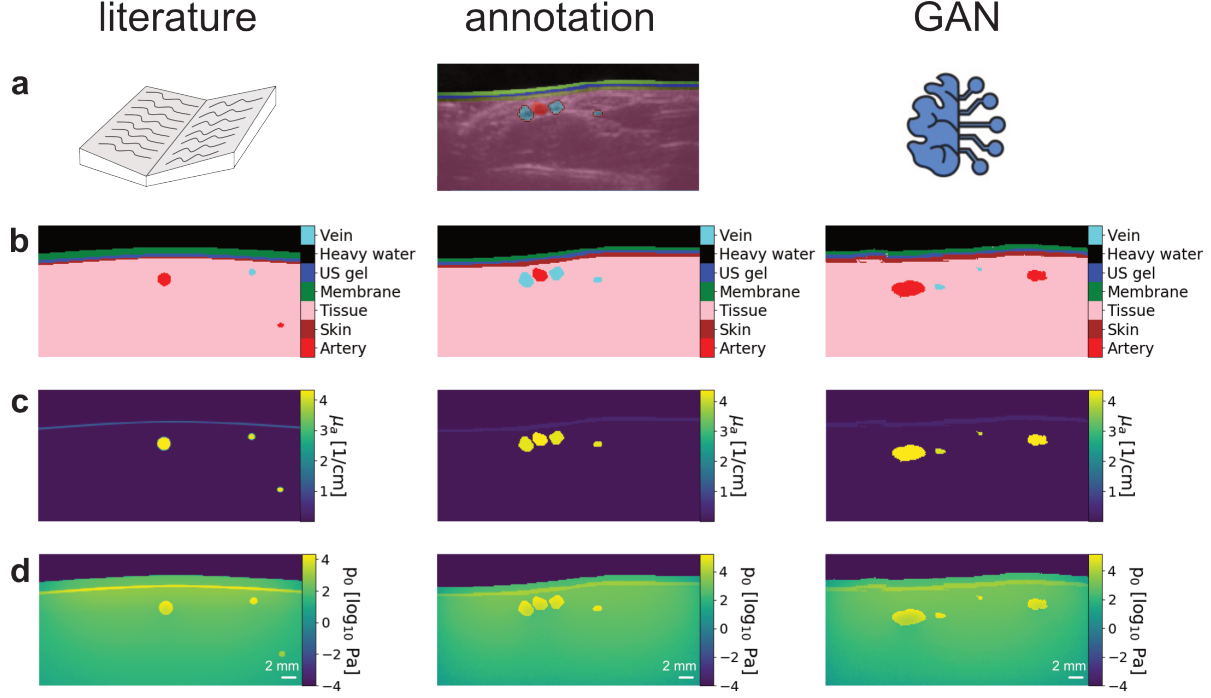


Figure 3: Examples of the (*left*) literature-based, (*center*) annotation-based, and (*right*) Generative Adversarial Network (GAN)-based parameter images. Leveraging (**a**) the respective anatomical information source, (**b**) the anatomical parameter images are generated and used to assign (**c**) the corresponding absorption coefficient μ_a (according to literature values of optical tissue parameters of a human forearm) which enables the simulation of (**d**) the initial pressure distribution p_0 (μ_a and p_0 here shown at 800 nm).

| Hyperparameter | Value |
|----------------------------|-------------------|
| max epochs | 1200 |
| batch size | 3 |
| instance noise std | 0.3 |
| label flipping | true |
| label flip p(start) | 0.2 |
| label flip linear decrease | true |
| generator | |
| learning rate | $2 \cdot 10^{-4}$ |
| initial filter size | 128 |
| discriminator | |
| learning rate | $2 \cdot 10^{-4}$ |
| initial filter size | 64 |

Table 2: Hyperparameters used for Generative Adversarial Network (GAN) training.

2.3.4 Comparative performance assessment

To investigate the benefit of our "learning-to-simulate" approach, we assessed the effect of the method for geometry generation on a downstream task, namely the reconstruction of the spatially-resolved optical absorption μ_a from PAT images. Our strategy involved training qPAT models, all of the same U-Net architecture, on data sets corresponding to the three strategies presented in sections 2.3.1 - 2.3.3 (literature-based, annotation-based, GAN-based), and combinations thereof. More specifically, we used five different configurations shown in Table 3 and subdivided the data into training (70%), validation (10%), and test data (20%). Note that the same annotations were used as a basis for

the annotation-based and GAN-based approaches. The GAN-based approach can thus be seen as a form of data augmentation.

Previous works [22] and a recent review on deep learning for biomedical PAT [7] have demonstrated that the U-Net architecture shows particular promise in tackling the optical inverse problem. The U-Net architecture applied is shown in Figure 4. The hyperparameters were determined by a grid search analysis on the corresponding validation data set (cf. Tab. 4). Test results were then determined on both the respective held-out test set as well as on the realistic annotation-based test set highlighted in green in Table 3.

| Dataset | Training 70 % | Validation 10 % | Test 20 % |
|--|------------------|--------------------|--------------|
| annotation-based | 42 | 6 | 12 |
| literature-based | 350 | 40 | 100 |
| GAN-based | 350 | 40 | 100 |
| combination of GAN- and annotation-based (90:10) | 350 | 40 | 100 |
| combination of literature-, GAN-, and annotation-based | 742 | 88 | 212 |

Table 3: Five different configurations of three data sets with respective training, validation, and test split. The target test data set is highlighted in green.

A quantitative analysis of the estimated absorption coefficients $\hat{\mu}_a$ on the respective test data set x was performed using the median relative error, $\widetilde{RE}_{x,\lambda}$, the median absolute error $\widetilde{AE}_{x,\lambda}$, and the structural similarity index (*SSIM*) [23]. The median relative and absolute errors are defined as:

$$\widetilde{RE}_{x,\lambda} = \text{median} \frac{|\hat{\mu}_{a,i,\lambda} - \mu_{a,i,\lambda}|}{|\mu_{a,i,\lambda}|}, \quad (1)$$

$$\widetilde{AE}_{x,\lambda} = \text{median} |\hat{\mu}_{a,i,\lambda} - \mu_{a,i,\lambda}|, \quad (2)$$

where x is the test data index, i is the pixel index, λ the evaluated wavelength, $\hat{\mu}_{a,i,\lambda}$ the estimated absorption coefficient at pixel i , and $\mu_{a,i,\lambda}$ the ground truth absorption coefficient at pixel i .

For comparison of the different techniques, we applied the *challengeR* method [24]. It is especially suited for analyzing and visualizing challenge results across different tasks in the field of biomedical image analysis. The challenge in our context is the performance of the downstream task. The competing algorithms were defined as the five algorithms corresponding to the training data sets presented in Table 3 (all processed with the same neural network model). As *tasks*, we defined the quantification of optical absorption for the different wavelengths ($n = 16$ in total). We then used the tool to compute performance images for the three different metrics \widetilde{AE} , \widetilde{RE} , and *SSIM*. In particular, the tool was used in the aggregate-then-rank mode to investigate the consensus ranking stability approach (default settings).

| Hyperparameter | Value |
|---------------------|-------------------|
| learning rate | $1 \cdot 10^{-4}$ |
| max epochs | 100 |
| batch size | 3 |
| initial filter size | 128 |
| downsampling steps | 2 |

Table 4: Hyperparameters used for U-Net training.

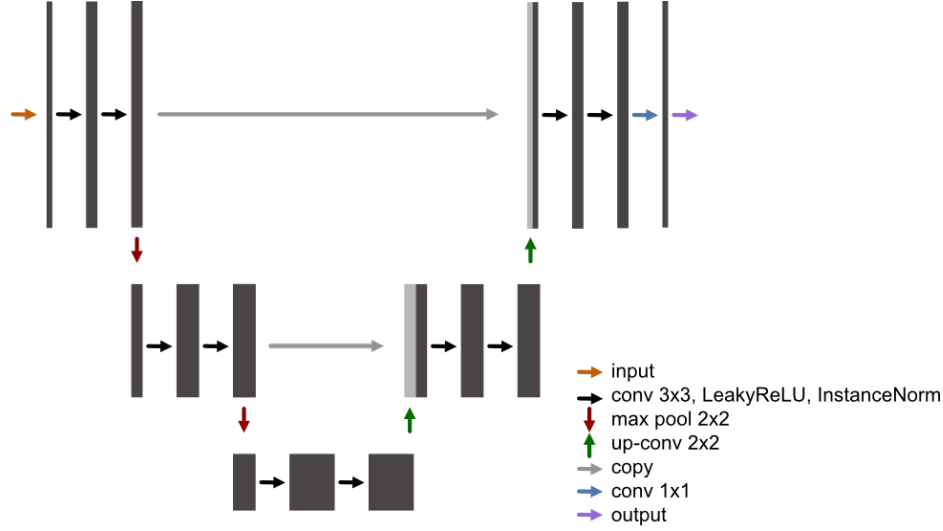


Figure 4: Network architecture of the U-Net based quantification model.

3 Results

The performance of the U-Net-based models trained on different configurations of the three data sets (cf. Tab. 3) are presented in Figures 5 and 6.

When tested on the same annotation-based data set, the data-driven methods clearly outperform the literature-based method that is exclusively based on prior knowledge (cf. Fig. 5). Leveraging the (larger) GAN-based data set also yields a substantial improvement compared to using only the annotations (without further augmentation). The best performance is achieved when combining all the available data. These findings hold true irrespective of the specific metric that is applied.

The median and interquartile range of the relative error for all methods and wavelengths are plotted in Figure 6 for both the (different) test sets reflecting the distribution of the respective training set and the joint (most realistic) test set. For both test sets, the median and interquartile range of the relative and absolute errors at 700 nm and 800 nm for three methods (literature-based, GAN-based, and annotation-based) are presented in Table 5. The results show that the performance is highly wavelength-dependent for all methods. Furthermore, the performance on held-out test data (in distribution) does not generalize to the (more realistic) joint test data for the literature-based method.

| | \widetilde{AE} (IQR) [1/cm] | | \widetilde{RE} (IQR) [%] | |
|------------------|-------------------------------|------------------|----------------------------|------------------|
| | held-out | annotation-based | held-out | annotation-based |
| 700 nm | | | | |
| literature-based | 1.3 (2.4) | 25.2 (30.5) | 3.0 (4.1) | 35.9 (48.6) |
| GAN-based | 3.8 (9.1) | 5.8 (11.1) | 8.1 (13.4) | 11.5 (16.6) |
| annotation-based | | 8.5 (26.6) | | 17.6 (37.9) |
| 800 nm | | | | |
| literature-based | 0.6 (1.1) | 1.1 (2.1) | 1.5 (2.1) | 3.1 (5.5) |
| GAN-based | 0.6 (1.1) | 0.6 (1.2) | 1.4 (2.0) | 1.5 (2.0) |
| annotation-based | | 2.1 (0.4) | | 4.9 (7.0) |

Table 5: The median of the absolute and relative errors (\widetilde{AE} and \widetilde{RE}) and the corresponding interquartile range (IQR) at 700 nm and 800 nm for the literature-based, Generative Adversarial Network (GAN)-based, and annotation-based methods tested on both, the (different) held-out test sets reflecting the distribution of the respective training set and the joint annotation-based test set. In contrast to the literature-based model, the GAN-based model performs similarly when applied on the held-out or realistic annotation-based test set.

Qualitative results for three of the models on the same test data are shown in Figure 7. The presented image was chosen according to the median \widetilde{RE}_{700nm} for the model trained on the literature-based data set. The estimated

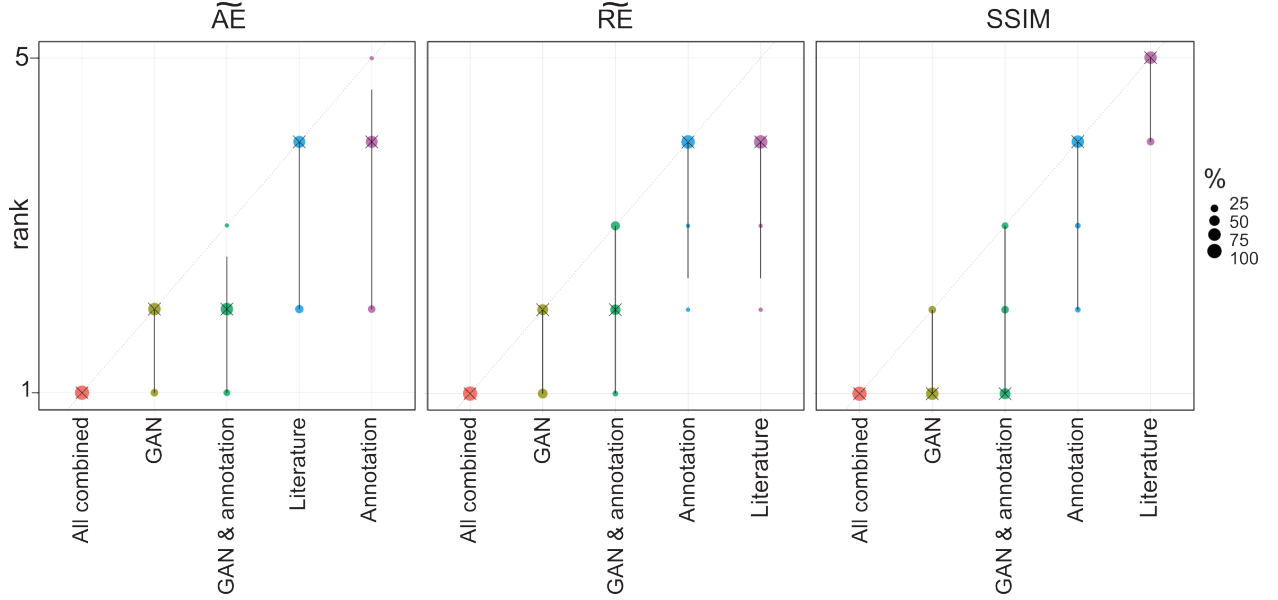


Figure 5: Comparative performance assessment of the models corresponding to different training sets and tested on identical annotation-based test data. Uncertainty-aware rankings were computed for the median absolute error (\widetilde{AE}), median relative error (\widetilde{RE}), and structural similarity index (SSIM) using the *challengeR* concept [24]. The area of each blob at position ($Method_i$, rank j) is proportional to the relative frequency $Method_i$ achieved rank j , where individual *tasks* (for which rankings are computed) correspond to the solving of the optical inverse problem for different wavelengths. The median rank for each model is indicated by a black cross. The black lines indicate 95% confidence intervals ranging (from the 2.5th to the 97.5th percentile).

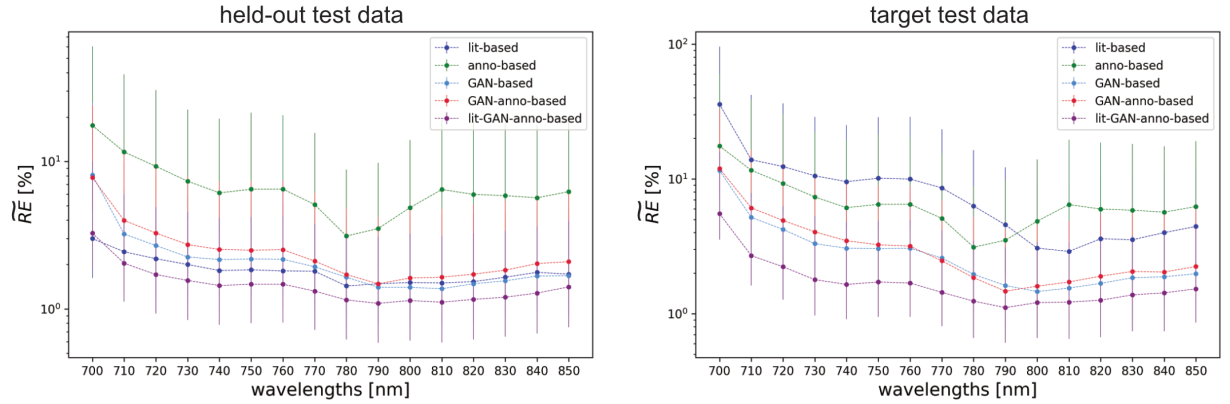


Figure 6: Quantitative results of the same U-net model trained on the five different data sets shown in Tab. 3. (*Left*) The median and interquartile range of the relative errors of the respective in distribution held-out test set and their dependencies on the wavelengths are shown for every model. The median relative errors of all models are dependent on the wavelengths and (except for the annotation-based model) in the same range of the order of magnitude. (*Right*) The median and interquartile range of the relative errors of the annotation-based target test data and their dependency on the wavelengths are shown for every model.

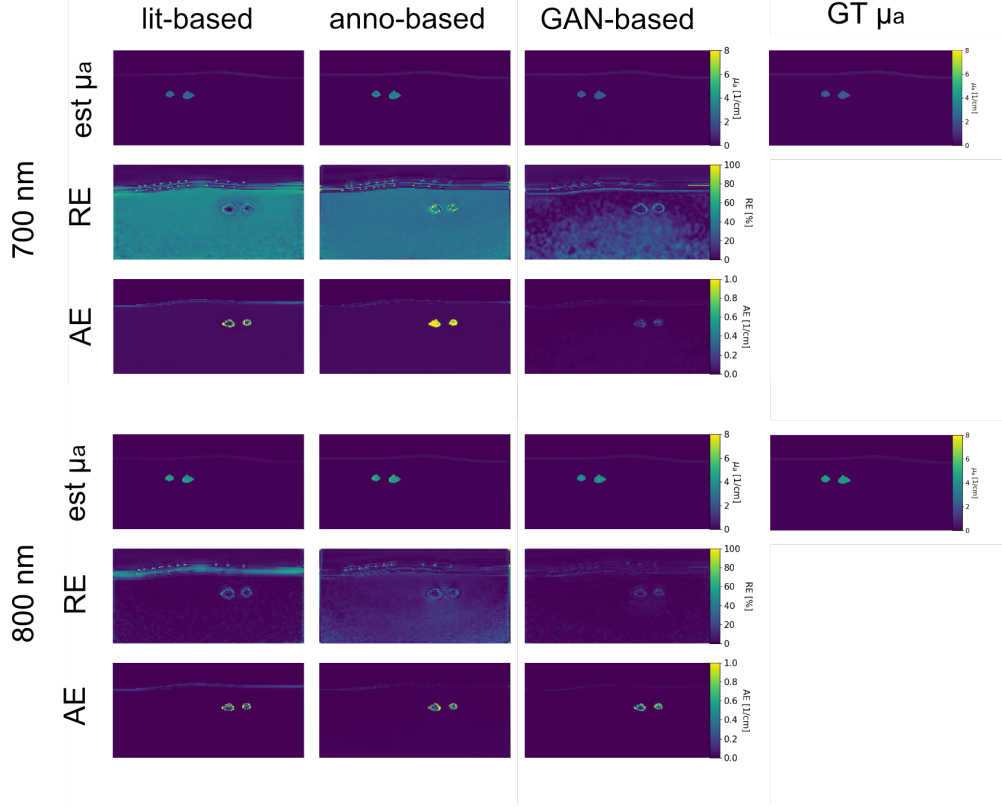


Figure 7: Qualitative results on a representative test case (annotation-based) at (*top*) 700 nm and (*bottom*) 800 nm. The estimated absorption coefficient ($\text{est } \mu_a$), the relative error (RE), the absolute error (AE), and the corresponding ground truth (GT μ_a) are shown for the models trained on annotation-based (anno), literature-based (lit), and Generative Adversarial Network (GAN)-based data. The μ_a estimations of the models including GAN-based data most closely resemble the μ_a GTs. However, the errors are high for all three models, especially within the skin and vessels.

absorption coefficients differ visually from the ground truth coefficients for the models trained on literature-based or annotation-based data sets. The estimations of the models trained on data including GAN-based data more closely resemble the ground truth coefficients, especially visible at 700 nm (cf. Fig. 6). However, the relative error images show that all models perform worse at 700 nm compared to at 800 nm. Especially within skin and vessels, the estimated absorption coefficients at 700 nm are error-prone for all models.

4 Discussion

In this work, we proposed the NEURAL SPICING approach to qPAT (NS-qPAT) as a novel framework for photoacoustic image analysis relying on two pillars: (1) the explicit disentanglement of different factors contributing to image formation and (2) the data-driven approach to image synthesis (“learning to simulate”). With the present contribution, we are, to our knowledge, the first to apply an adversarial approach to the simulation of realistic tissue geometries in the specific context of PAT. Our initial feasibility study suggests that the proposed data-driven approach is better suited for PAT tissue synthesis compared to the traditional model-based approach.

Although the annotated tissue geometries can be expected to resemble the test data geometries the most due to the same underlying data distribution, the performance of the corresponding model was worse compared to those of the other methods (literature-based and GAN-based). The most plausible explanation for this phenomenon, based on our data, is the small data set size, thus confirming the need for realistic image synthesis. The fact that the GAN-based methods performed so well compared to the literature-based method indicates that we were able to generate realistic anatomical parameter images in a data-driven manner.

It should further be mentioned in this context that combining the annotation-based set with the GAN-based set can essentially be interpreted as a form of data augmentation. Data augmentation in qPAT is in fact non-trivial, as the standard mechanisms (e.g., image translation, rotation, scaling) are not applicable because they would alter the reference annotations of the optical parameters. Here, we overcame this problem by disentangling the geometry from the optical and acoustic properties. This enabled us to perform the augmentation of geometry before the actual photon simulation.

In the presented study, the data set that the GAN training was based on was relatively small. To compensate for this, we included a post-processing step in which we excluded implausible geometries generated by the GAN. Note that this manual exclusion is substantially less time-consuming compared to semantic image segmentation and can potentially be omitted/reduced to a minimum of work in cases when the GAN is trained on more data.

The quantitative results of the U-Net-based quantification model tested on held-out test data of the different *in silico* data sets (cf. left plot in Fig. 6) indicate the general suitability of this architecture in estimating the absorption coefficient μ_a from the initial pressure p_0 . Even though no further optimizations except for a hyperparameter optimization by the applied grid search were performed, our simple model shows comparable performances with previous machine learning-based approaches for solving the optical inverse problem [22, 25, 26]. Also, neither extensive data augmentation nor model ensembling - both traditional performance boosts - were applied in this work. It should further be noted that all models were trained on single wavelength images. Future work should be directed to jointly analyzing all wavelengths for addressing the optical inverse problem.

All models showed a quantification performance that was dependent on the wavelengths when tested on both in distribution held-out data and annotation-based target test data (cf. Fig. 6 and Fig. 7). This behavior could be a consequence of an imbalance between different tissue classes. For example, the amount of pixels assigned to the skin or vein classes is small compared to the background tissue class. We assume the model to learn a mapping of signal intensities to the underlying absorption coefficients. Since the signal intensity of melanin (primarily in the skin) and deoxygenated hemoglobin (primarily in venous blood) is at a maximum at 700 nm, the difference in performance is especially large at that wavelength.

In this work, we chose the commonly applied median relative error as a performance metric. This error increases non-linearly with increasingly smaller underlying parameters, which, in turn, causes the values to be relatively large in regions of small absorption coefficients. To compensate for this effect, we additionally used the absolute error and the SSIM, but the conclusions drawn from the experiments corresponding to the three different metrics were identical.

A limitation of our approach could be seen in the fact that we have no guarantee for our anatomical parameter images to accurately reflect tissue geometries. One reason for this is that the annotations were performed on US and PAT data - both modalities that require experience in image interpretation and are highly dependent on the quality of the reconstruction algorithm. However, our general concept is not at all limited to these modalities and could instead be applied to better interpretable images, such as CT or MRI. Furthermore, the optical properties assigned to the parameter images do not reflect the full spectrum of tissue property variations that can occur in practice. Despite these issues, we see the strength of our approach by the fact that we managed to disentangle performance effects that can be attributed to the tissue geometry from those resulting from the optical properties themselves. With this concept, we are the first to show that the performance of DL-based qPAT solutions depends crucially on the method used to generate tissue geometries.

Overall, we believe that the proposed "learning to simulate" approach has high potential to enhance the realism of synthetic PAT data and could thus become an important concept for generating adequate training data for qPAT applications as well as for generating realistic validation data in the field.

5 Declarations

Funding: This project was funded by the Data Science Driven Surgical Oncology Program of the National Center for Tumor Diseases (NCT) Heidelberg and was conducted in the scope of the NEURAL SPICING grant, funded by the European Research Council (ERC) under the European Union’s Horizon 2020 research and innovation programme (grant agreement No. [101002198]).

Conflicts of interest: The authors declare that they have no conflict of interest.

Ethics approval: The healthy human volunteer experiments were approved by the ethics committee of the medical faculty of Heidelberg University under reference number S-451/2020 and the study is registered with the German Clinical Trials Register under reference number DRKS00023205.

Availability of data/code, material, and annotation protocol: Available upon request.

References

- [1] L. V. Wang and L. Gao, “Photoacoustic microscopy and computed tomography: From bench to bedside,” *Annual Review of Biomedical Engineering* **16**(1), pp. 155–185, 2014. PMID: 24905877.
- [2] P. Beard, “Biomedical photoacoustic imaging,” *Interface Focus* **1**(4), pp. 602–631, 2011.
- [3] A. B. E. Attia, G. Balasundaram, M. Moothanchery, U. Dinish, R. Bi, V. Ntziachristos, and M. Olivo, “A review of clinical photoacoustic imaging: Current and future trends,” *Photoacoustics* **16**, p. 100144, 2019.
- [4] B. T. Cox, S. R. Arridge, K. P. Köstli, and P. C. Beard, “Two-dimensional quantitative photoacoustic image reconstruction of absorption distributions in scattering media by use of a simple iterative method,” *Appl. Opt.* **45**, pp. 1866–1875, Mar 2006.
- [5] F. M. Brochu, J. Bruncker, J. Joseph, M. R. Tomaszewski, S. Morscher, and S. E. Bohndiek, “Towards quantitative evaluation of tissue absorption coefficients using light fluence correction in optoacoustic tomography,” *IEEE transactions on medical imaging* **36**(1), pp. 322–331, 2016.
- [6] C. Yang, H. Lan, F. Gao, and F. Gao, “Review of deep learning for photoacoustic imaging,” *Photoacoustics* **21**, p. 100215, 2021.
- [7] J. Gröhl, M. Schellenberg, K. Dreher, and L. Maier-Hein, “Deep learning for biomedical photoacoustic imaging: A review,” *Photoacoustics* **22**, p. 100241, 2021.
- [8] A. Hauptmann and B. T. Cox, “Deep learning in photoacoustic tomography: current approaches and future directions,” *Journal of Biomedical Optics* **25**(11), pp. 1 – 46, 2020.
- [9] I. Olefir, S. Tzoumas, C. Restivo, P. Mohajerani, L. Xing, and V. Ntziachristos, “Deep learning-based spectral unmixing for optoacoustic imaging of tissue oxygen saturation,” *IEEE Transactions on Medical Imaging* **39**(11), pp. 3643–3654, 2020.
- [10] K. K. Dreher, J. Gröhl, T. Adler, T. Krichner, and L. Maier-Hein, “Towards realistic simulation of photoacoustic images..” Photons Plus Ultrasound: Imaging and Sensing 2020 Conference Abstract, 2020.
- [11] T.-C. Wang, M.-Y. Liu, J.-Y. Zhu, A. Tao, J. Kautz, and B. Catanzaro, “High-resolution image synthesis and semantic manipulation with conditional gans,” in *Proceedings of the IEEE Conference on Computer Vision and Pattern Recognition (CVPR)*, June 2018.
- [12] J. Zhu, T. Park, P. Isola, and A. A. Efros, “Unpaired image-to-image translation using cycle-consistent adversarial networks,” *CoRR* **abs/1703.10593**, 2017.
- [13] P. Isola, J.-Y. Zhu, T. Zhou, and A. A. Efros, “Image-to-image translation with conditional adversarial networks,” 2018.
- [14] I. J. Goodfellow, J. Pouget-Abadie, M. Mirza, B. Xu, D. Warde-Farley, S. Ozair, A. Courville, and Y. Bengio, “Generative adversarial networks,” 2014.
- [15] A. Radford, L. Metz, and S. Chintala, “Unsupervised representation learning with deep convolutional generative adversarial networks,” 2016.
- [16] Y. Shin, J. Yang, and Y. H. Lee, “Deep generative adversarial networks: Applications in musculoskeletal imaging,” *Radiology: Artificial Intelligence* **0**(ja), p. e200157, 0.
- [17] J. Gröhl, T. Kirchner, T. J. Adler, L. Hacker, N. Holzwarth, A. Hernández-Aguilera, M. A. Herrera, E. Santos, S. E. Bohndiek, and L. Maier-Hein, “Learned spectral decoloring enables photoacoustic oximetry,” *Scientific reports* **11**(1), p. 6565, 2021.
- [18] Q. Fang and D. A. Boas, “Monte carlo simulation of photon migration in 3d turbid media accelerated by graphics processing units,” *Opt. Express* **17**, pp. 20178–20190, Oct 2009.
- [19] J. Gröhl, K. K. Dreher, M. Schellenberg, A. Seitel, and L. Maier-Hein, “Simpa: an open source toolkit for simulation and processing of photoacoustic images.” Poster presented at the meeting of the International Society for optics and photonics (SPIE), Photonics West BiOS, Paper 11642-71, 2021.
- [20] J. Gröhl, M. Schellenberg, K. K. Dreher, N. Holzwarth, M. D. Tizabi, A. Seitel, and L. Maier-Hein, “Semantic segmentation of multispectral photoacoustic images using deep learning..” Photons Plus Ultrasound: Imaging and Sensing 2021 Conference Abstract, 2021.
- [21] T. Kirchner, J. Gröhl, and L. Maier-Hein, “Context encoding enables machine learning-based quantitative photoacoustics,” *Journal of biomedical optics* **23**(5), p. 056008, 2018.
- [22] J. Gröhl, T. Kirchner, T. Adler, and L. Maier-Hein, “Confidence estimation for machine learning-based quantitative photoacoustics,” *Journal of Imaging* **4**(12), 2018.

- [23] Zhou Wang, A. C. Bovik, H. R. Sheikh, and E. P. Simoncelli, “Image quality assessment: from error visibility to structural similarity,” *IEEE Transactions on Image Processing* **13**(4), pp. 600–612, 2004.
- [24] M. Wiesenfarth, A. Reinke, B. A. Landman, M. Eisenmann, L. A. Saiz, M. J. Cardoso, L. Maier-Hein, and A. Kopp-Schneider, “Methods and open-source toolkit for analyzing and visualizing challenge results,” *Scientific Reports* **11**(1), pp. 1–15, 2021.
- [25] C. Cai, K. Deng, C. Ma, and J. Luo, “End-to-end deep neural network for optical inversion in quantitative photoacoustic imaging,” *Opt. Lett.* **43**, pp. 2752–2755, Jun 2018.
- [26] T. Chen, T. Lu, S. Song, S. Miao, F. Gao, and J. Li, “A deep learning method based on U-Net for quantitative photoacoustic imaging,” in *Photons Plus Ultrasound: Imaging and Sensing 2020*, A. A. Oraevsky and L. V. Wang, eds., **11240**, pp. 216 – 223, International Society for Optics and Photonics, SPIE, 2020.